

Classification of Filament Formation Mechanisms in Magnetized Molecular Clouds

DAISEI ABE,¹ TSUYOSHI INOUE,¹ SHU-ICHIRO INUTSUKA,¹ AND TOMOAKI MATSUMOTO²

¹*Department of Physics, Graduate School of Science, Nagoya University, Furo-cho, Chikusa-ku, Nagoya 464-8602, Japan*

²*Faculty of Humanity and Environment, Hosei University, Fujimi, Chiyoda-ku, Tokyo 102-8160, Japan*

(Received July 13, 2022; Accepted –)

Submitted to ApJ

ABSTRACT

Recent observations of molecular clouds show that dense filaments are the sites of present-day star formation. Thus, it is necessary to understand the filament formation process because these filaments provide the initial condition for star formation. Theoretical research suggests that shock waves in molecular clouds trigger filament formation. Since several different mechanisms have been proposed for filament formation, the formation mechanism of the observed star-forming filaments requires clarification. In the present study, we perform a series of isothermal magnetohydrodynamics simulations of filament formation. We focus on the influences of shock velocity and turbulence on the formation mechanism and identified three different mechanisms for the filament formation. The results indicate that when the shock is fast, at shock velocity $v_{\text{sh}} \simeq 7 \text{ km s}^{-1}$, the gas flows driven by the curved shock wave create filaments irrespective of the presence of turbulence and self-gravity. However, at a slow shock velocity $v_{\text{sh}} \simeq 2.5 \text{ km s}^{-1}$, the compressive flow component involved in the initial turbulence induces filament formation. When both the shock velocities and turbulence are low, the self-gravity in the shock-compressed sheet becomes important for filament formation. Moreover, we analyzed the line-mass distribution of the filaments and showed that strong shock waves can naturally create high-line-mass filaments such as those observed in the massive star-forming regions in a short time. We conclude that the dominant filament formation mode changes with the velocity of the shock wave triggering the filament formation.

Keywords: stars: formation — ISM: clouds — magnetohydrodynamics (MHD)

1. INTRODUCTION

Stars are formed in dense regions in molecular clouds (e.g., [Lada et al. 2010](#); [Enoch et al. 2007](#)). Recent observations by the *Herschel* space telescope revealed that dense filamentary structures are ubiquitous in nearby molecular clouds (e.g., [André et al. 2010](#); [Arzoumanian et al. 2011](#)). Additionally, star-forming cores and young stellar objects are embedded along the filaments, which indicate their crucial role in star formation ([Könyves et al. 2015](#)). To create stars in filaments, their line-masses exceed the critical line-mass for gravitational instability, $M_{\text{line,cr}} = 2c_s^2/G \simeq 17 \text{ M}_{\odot} \text{ pc}^{-1}$, where $c_s \simeq 0.2 \text{ km s}^{-1}$ is the isothermal sound speed of

typical molecular clouds (e.g., [Stodólkiewicz 1963](#); [Ostriker 1964](#)).

Theoretical research about filament formation proposes three mechanism types. Regarding the first type, several studies discuss filament creation by self-gravitational fragmentation of a sheetlike cloud ([Tomisaka & Ikeuchi 1983](#); [Miyama et al. 1987a,b](#); [Nagai et al. 1998](#); [Kitsionas & Whitworth 2007](#); [Balfour et al. 2015, 2017](#)) created when molecular clouds are shock-compressed. Such compression naturally occurs owing to cloud-cloud collision, feedback from massive stars including supernovae and expanding HII regions, and encounters with galactic spiral shock. All of these processes induce shock waves in molecular clouds. According to linear stability analysis by conducted [Nagai et al. \(1998\)](#), gravitational instability creates filaments with line-masses several times greater than the critical

line-mass when the width of the sheet is roughly larger than its scale height.

For the second type, Padoan & Nordlund (1999), Chen & Ostriker (2014), Chen (2015), Matsumoto et al. (2015), and, Federrath (2016) showed filament formation induced by turbulence in molecular clouds by using three-dimensional magnetohydrodynamic (MHD) simulation. Padoan & Nordlund (1999) reported that the turbulent velocity given in an initially uniform molecular gas induces the formation of shock-compressed sheets, the interaction of which creates filaments. It should be noted that this process occurs in the super-Alfvénic case, in which the initial Alfvénic Mach number $\mathcal{M}_{A,i} \sim 10$. In the trans-Alfvénic case ($\mathcal{M}_{A,i} \sim 1$), they also found that filaments are formed by gas flows converging along the magnetic field. This mechanism creates the filaments that are perpendicular to the background magnetic field when the turbulence is sub-Alfvénic (Chen & Ostriker 2014; Chen 2015; Planck Collaboration XXXV 2016). This is because the component of turbulent velocity perpendicular to the magnetic field is suppressed by magnetic tension force, and only motion parallel to the magnetic field can compress the gas. In the present study, we refer to such turbulence-induced mechanisms as turbulent filament formation. Hennebelle (2013) reported that a small clump in a turbulent molecular cloud is stretched by turbulent shear flows and evolves into a small line-mass filament parallel to the magnetic field (see also Inoue & Inutsuka 2016, for the origin of HI filament/fiber).

Regarding the third type, Inoue & Fukui (2013), Vaidya et al. (2013), and Inoue et al. (2018) reported that the filaments are generated when a shock wave sweeps a cloud containing density inhomogeneity or clumps. In this case, a dense blob embedded in a magnetized molecular cloud is transformed into a dense filament in the shock-compressed layer. It should be noted that the effects of the thermal instability and turbulence cause molecular clouds to be generally highly clumpy by nature (e.g., Inoue & Inutsuka 2012). We stress that in most theoretical works that study structure formation in molecular clouds by turbulence, a uniform density cloud is assumed as an initial condition. Therefore the filamentation mode pointed out by Inoue & Fukui (2013) is omitted when considering the uniform density initial condition. As we show subsequently, this filamentation mode dominates over other modes when the shock Mach number is high. Throughout this study, this filament formation mode is called as an oblique MHD shock compression mechanism because oblique MHD shock plays a crucial role in the filament formation.

Although many different filament formation mechanisms have been proposed, as discussed above, the most realistic or most effective mechanism for star formation remains unknown. Most of the proposed mechanisms are triggered by shock compression: thus, we perform in this study a series of isothermal MHD simulations of filament formation by shock waves, focusing on the influences of shock strength, turbulence, and self-gravity on the filament formation mechanism. In addition, we analyze the line-mass distribution of the simulated filaments.

The paper is organized as follows. In §2, we provide the setup of our simulations. In §3, we give and interpret the results, and we analyze the filament line-mass distribution. In §4, simple models are presented that account for the dominant filament formation timescale. Finally, we summarize the results in §5.

2. SETUP OF SIMULATIONS

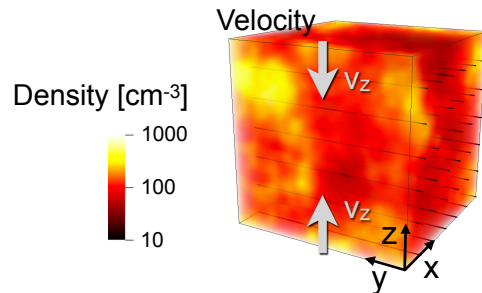


Figure 1. Schematic diagram of initial condition. The color bar represents the density magnitude; the black lines are the initial magnetic field lines; and the grey arrows indicate the orientations of the converging flows.

We solve the isothermal MHD equations with self-gravity by using the SFUMATO code (Matsumoto 2007) in which the MHD equations are integrated by using a Godunov-type scheme with a HLLD Riemann solver (Miyoshi & Kusano 2005) having third- and second-order accuracies in space and time, respectively. A divergence cleaning method (Dedner et al. 2002) ensures the divergence free condition, $\nabla \cdot \mathbf{B} = 0$. Poisson’s equation is solved by using the multi-grid method.

We investigate the mechanism of filament formation induced by shock waves by performing converging flow simulations. A schematic illustration of the initial condition is shown in Figure 1. We prepare a cubic numerical domain of side lengths $L_{\text{box}} = 6.0$ pc consisting of 512^3 uniform numerical cells, indicating that the physical resolution Δx is approximately 0.012 pc. We initially set the isothermal gas characterized by the isothermal sound speed at $c_s = 0.2$ km s $^{-1}$. Because molecular

Table 1. Model parameters.

Model Name	Collision Velocity v_{coll} [km s $^{-1}$]	Shock Velocity v_{sh} [km s $^{-1}$]	Self-Gravity	Turbulence
v12GyTn	12	7.0	Yes	No
v12GnTn	12	7.0	No	No
v12GyTy	12	7.0	Yes	Yes
v12GnTy	12	7.0	No	Yes
v10GyTn	10	6.0	Yes	No
v8GyTn	8.0	5.0	Yes	No
v6GyTn	6.0	4.0	Yes	No
v3GyTn	3.0	2.5	Yes	No
v3GnTn	3.0	2.5	No	No
v3GyTy	3.0	2.5	Yes	Yes
v3GnTy	3.0	2.5	No	Yes

NOTE—Gas continuously flows into the calculation box from the upper and lower boundaries and initially collides at $z = 3$ pc with the relative velocity v_{coll} . After the collision the shock velocity v_{sh} in the rest frame of the upstream gas becomes larger than $v_{\text{coll}}/2$, and thus, the thickness of the shock-compressed layer expands. We show the relation between collision velocity and shock velocity in Eqs. 2

clouds are highly inhomogeneous by nature, we initially add isotropic density fluctuations given as a superposition of sinusoidal functions with various wavenumbers from $2\pi/L_{\text{box}} \leq |k| \leq 32\pi/L_{\text{box}}$ and random phases. The power spectrum of the density fluctuations is given by $(\log \rho)_k^2 \propto k^{-4}$, which can be expected as a consequence of supersonic turbulence (Beresnyak et al. 2005; Elmegreen & Scalo 2004; Scalo & Elmegreen 2004; Larson 1981; Heyer & Brunt 2004). Thus, the initial density structure of our simulations is parameterized by mean density $\bar{n}_0 = \bar{\rho}_0/m = 100 \text{ cm}^{-3}$ and dispersion $\Delta n/\bar{n}_0 = 0.5$, where $\bar{\rho}_0$ and $m = 2.4 m_{\text{proton}}$ are the mean mass density and the mean mass of the molecular gas particles, respectively. In addition to density fluctuations, we set the initial turbulent velocity field to depend on the model summarized in Table 1. The initial turbulent velocity fluctuation has a dispersion of 1.0 km s^{-1} with a power spectrum of $v_k^2 \propto k^{-4}$ following Larson’s law (Larson 1981).

In addition to the turbulent component, we set the initial coherent velocity component as $v_z(z) = -(v_{\text{coll}}/2) \tanh[z - 3]$, i.e., two flows colliding head-on in the x-y plane at the center of the numerical domain ($z = 3$ pc) with a relative velocity of v_{coll} . In the previous studies of turbulent filament formation mentioned in §1, the filaments are created in the shock-compressed layer with shock velocity a few kilometers per second. In the oblique MHD shock compression mechanism, however, the filament formation is studied for high shock velocity cases of $\sim 10 \text{ km s}^{-1}$. To systematically study the filament formation mechanism, we perform simulations using different shock velocities. Specifically, we examine cases with $v_{\text{coll}} = 3$, $v_{\text{coll}} = 6$, $v_{\text{coll}} = 8$, $v_{\text{coll}} = 10$, and

12 km s^{-1} . Table 1 includes a summary of the model parameters. In the model names, the number following “v” represents the value of v_{coll} in units of km s^{-1} , and the characters “y” and “n” following “G” and “T” represent simulation with and without self-gravity and initial turbulence, respectively.

At the x-y boundary planes, the velocity is fixed at $v_{\text{coll}}/2$, and the density is given by $n_0(x, y, z = v_{\text{coll}}t/2)$ for the $z = 6$ pc plane and $n_0(x, y, z = L_{\text{box}} - v_{\text{coll}}t/2)$ for the $z = 0$ pc plane, where $n_0(x, y, z)$ is the initial density field including fluctuations. For the z-x and y-z boundary planes, we impose periodic boundary conditions.

We initially set a uniform magnetic field of $\mathbf{B}_0 = (0, 10 \mu\text{G}, 0)$, which is perpendicular to the direction of the shock propagation. This magnetic field strength is consistent with observed magnitude in molecular clouds (e.g., Crutcher 2012; Heiles & Crutcher 2005). Because the magnetic field component perpendicular to the direction of the shock propagation is expected to be strongly amplified by the shock compression, whereas the parallel component is not, the initial z-component of the magnetic field would play a minor role even if it is given.

To investigate its effect on filament formation, we also perform simulations with and without self-gravity. When we take into account the self-gravity, we use the sink particle technique in the regions in which gravitational collapse is expected to occur. The sink particle generation condition is the same as that discussed in previous research (Inoue et al. 2018; Matsumoto et al. 2015). It should be noted that the employment of the sink particle is simply for a continuation of the simu-

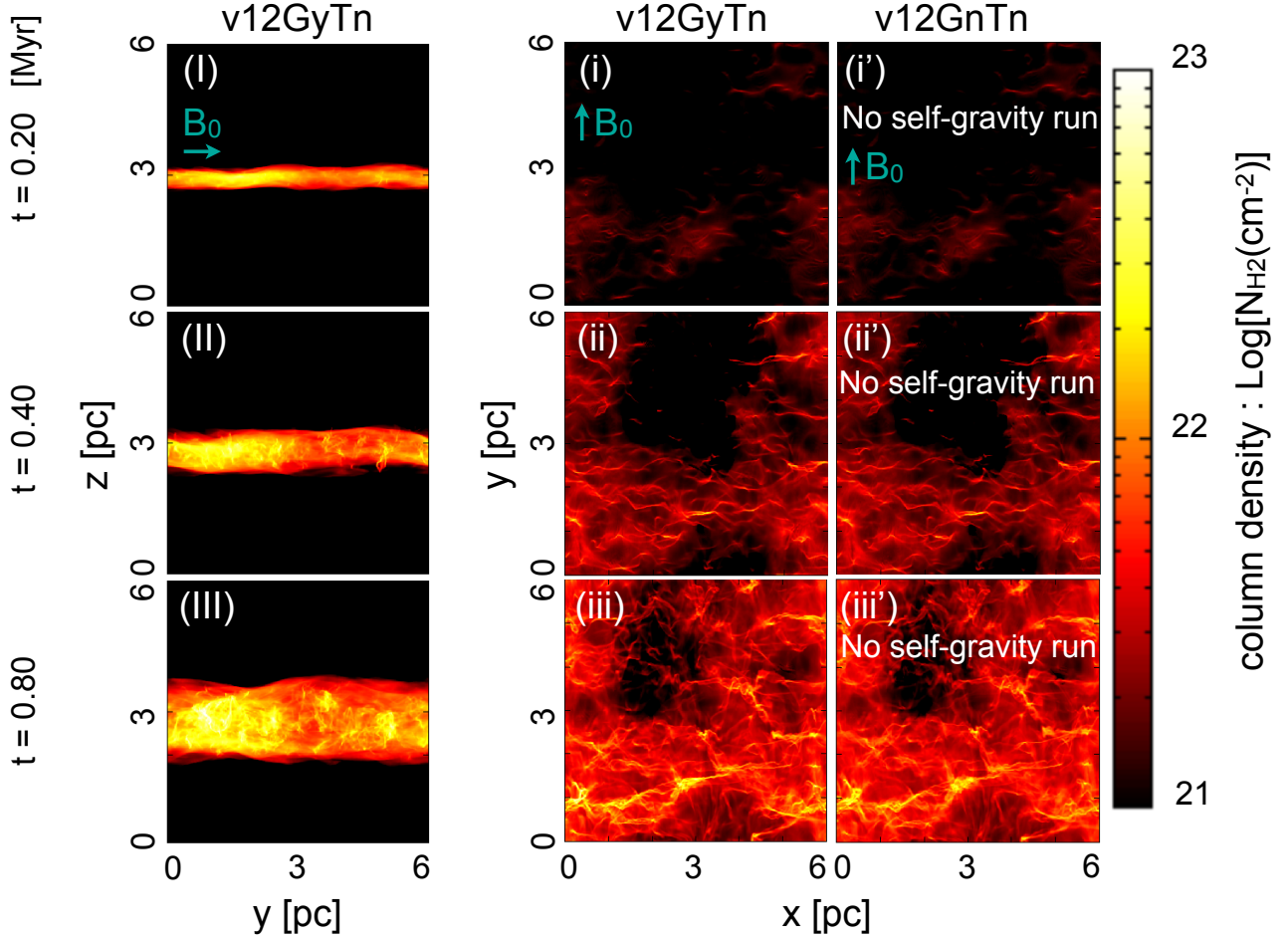


Figure 2. Column density maps at time $t = 0.2$ (top), 0.4 (middle), and 0.8 (bottom) Myr. *Left row* (panels I, II, and III): Column density in the y - z plane of model v12GyTn. *Middle row* (panels i, ii, and iii): Same as panels (I)-(III) but for the x - y plane. *Right row* (panels i', ii', and iii'): Same as panels (i)-(iii) but for model v12GnTn.

lations even after onset of local gravitational collapse¹. In this paper, we will not focus on the information of sink particles, because resulting total mass of the sink particles are much smaller than that of dense filaments (for instance, the final total mass of the sink particles is only 3% to that of dense filaments for model v12GyTy, and 6% for model v3GyTy).

3. RESULTS

3.1. High Shock Velocity Case

In the case of $v_{\text{coll}} = 12 \text{ km s}^{-1}$, the flow collision induces fast isothermal MHD shock waves. According

to the shock jump condition: $\rho_0 v_0^2 \sim B_1^2 / (8\pi)$ (e.g., §4.1 of Fukui et al. 2020), the compression ratio is given by

$$\rho_1 / \rho_0 = v_0 / v_1 \simeq \sqrt{2} \mathcal{M}_A, \quad (1)$$

where $\mathcal{M}_A \equiv v_0 / v_{\text{Alf},0}$ is the Alfvénic Mach number, the Alfvén velocity is given by $v_{\text{Alf},0} = B_0 / \sqrt{4\pi\rho_0}$ and B_1 is the magnetic field strength in the post-shock region. The pre-shock velocity in the shock rest-frame v_0 is equivalent to the shock velocity in the upstream rest frame v_{sh} . Given that the numerical domain is on the post-shock rest frame, the shock wave propagates with the velocity of $v_1 \simeq v_0 / (\sqrt{2} \mathcal{M}_A)$. The relation between the converging flow velocity v_{coll} and the shock velocity v_{sh} is given by

$$\begin{aligned} v_{\text{sh}} &= v_{\text{coll}}/2 + v_1 \\ &\simeq v_{\text{coll}}/2 + v_{\text{Alf},0}/\sqrt{2} \\ &\simeq 6 \left(\frac{v_{\text{coll}}}{12 \text{ km s}^{-1}} \right) \text{ km s}^{-1} \end{aligned}$$

¹ The threshold density for the sink formation is $5.6 \times 10^4 \text{ cm}^{-3}$. This value is much lower than that used in our previous studies, because we do not employ the adaptive mesh refinement in the present study

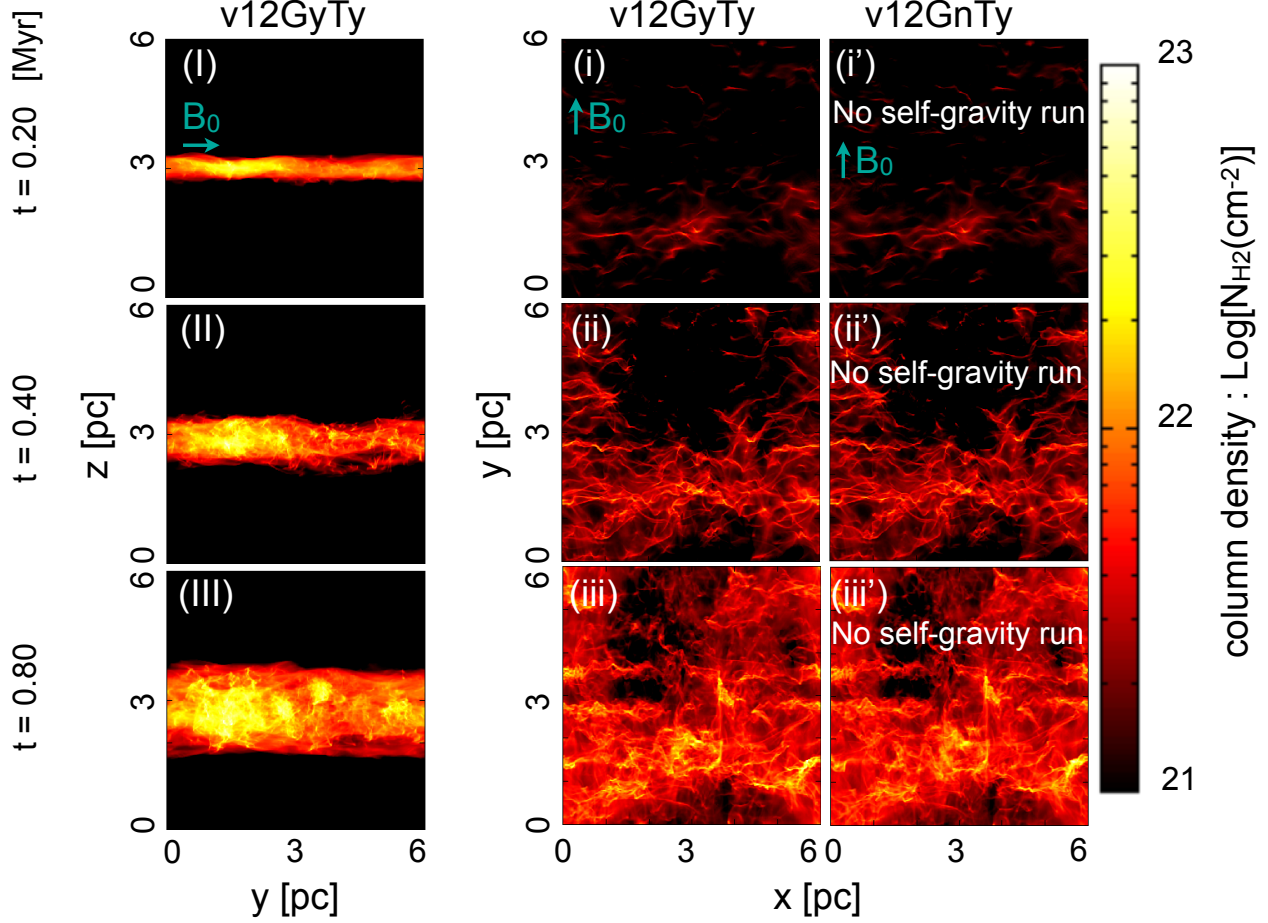


Figure 3. Column density maps at time $t = 0.2$ (top), 0.4 (middle), and 0.8 (bottom) Myr. *Left row* (panels I, II, and III): Column density in the y - z plane of model v12GyTy. *Middle row* (panels i, ii, and iii): Same as panels (I)-(III) but for the x - y plane. *Right row* (panels i', ii', and iii'): Same as panels (i)-(iii) but for model v12GnTy.

$$+1 \left(\frac{B_0}{10 \mu\text{G}} \right) \left(\frac{n_0}{100 \text{ cm}^{-3}} \right)^{-1/2} \text{ km s}^{-1}. \quad (2)$$

In Figure 2, we show snapshots of the column density structure as the results of models v12GyTn and v12GnTn at $t = 0.2$ (top), 0.40 (middle), and 0.60 (bottom) Myr. In constructing the column density, we identify the shock fronts and integrate them only in the shock-compressed region. To identify the shock fronts, we scan the total pressure $\rho(x, y, z)c_s^2 + B^2(x, y, z)/8\pi$ along the z -axis from upstream ($z = 0$ and 6) to downstream ($z = 3$) and define the two shock fronts as the largest and smallest locations of $z(x, y)$ where the following condition is satisfied:

$$\rho(x, y, z)c_s^2 + B^2(x, y, z)/8\pi \geq f_{\text{jump}} \times \bar{\rho}_0 v_{\text{coll}}^2, \quad (3)$$

where we choose $f_{\text{jump}} = 0.2$ for convenience, but we confirmed that the result with $f_{\text{jump}}=0.4$ gives the indistinguishable result.

Panels (I)-(III) and (i)-(iii) in Figure 2 show column density snapshots of model v12GyTn in the y - z and x - y planes, respectively. Panels (I), (II), and (III) show two shock waves induced by the converging flows propagating toward the positive and negative z -directions. Panels (i)-(iii) and (i')-(iii') show the formation of many filaments regardless of the effect of self-gravity, which indicates that the filament formation is not driven by self-gravity in the present high shock velocity cases. In §3.4, we show that very massive filaments as large as $100 M_\odot \text{ pc}^{-1}$ are formed at $t = 1$ Myr.

Because the present models (v12GyTn and v12GnTn) do not include initial turbulence, the oblique MHD shock compression mechanism definitively accounts for the filament formation.

In Figure 3, we show snapshots at $t = 0.20$ (top), 0.40 (middle), and 0.60 (bottom) Myr of models v12GyTy (panels I-III and i-iii) and v12GnTy (panels i'-iii'). In

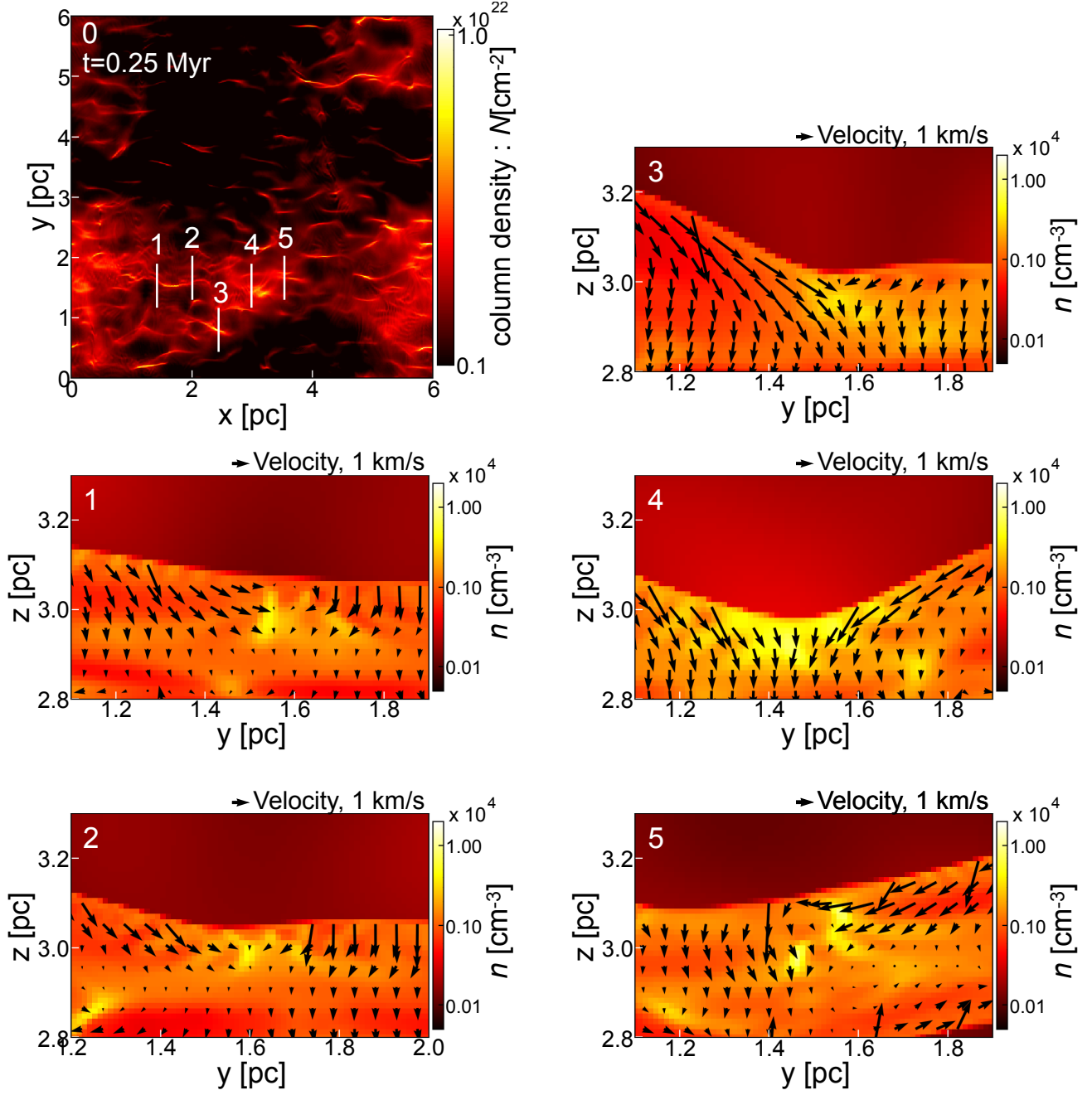


Figure 4. Panel (0): Early stage ($t = 0.25$ Myr) column density map in the x - y plane of result of model v12GyTn. The five white lines mark the planes in which the cross-section maps in panels (1)-(5) are drawn. Panels (1)-(5): Cross-section maps of the number density in the y - z plane. The yellow blobs located roughly at the center of each panel correspond to cross-sections of the filaments formed by the oblique MHD shock compression mechanism.

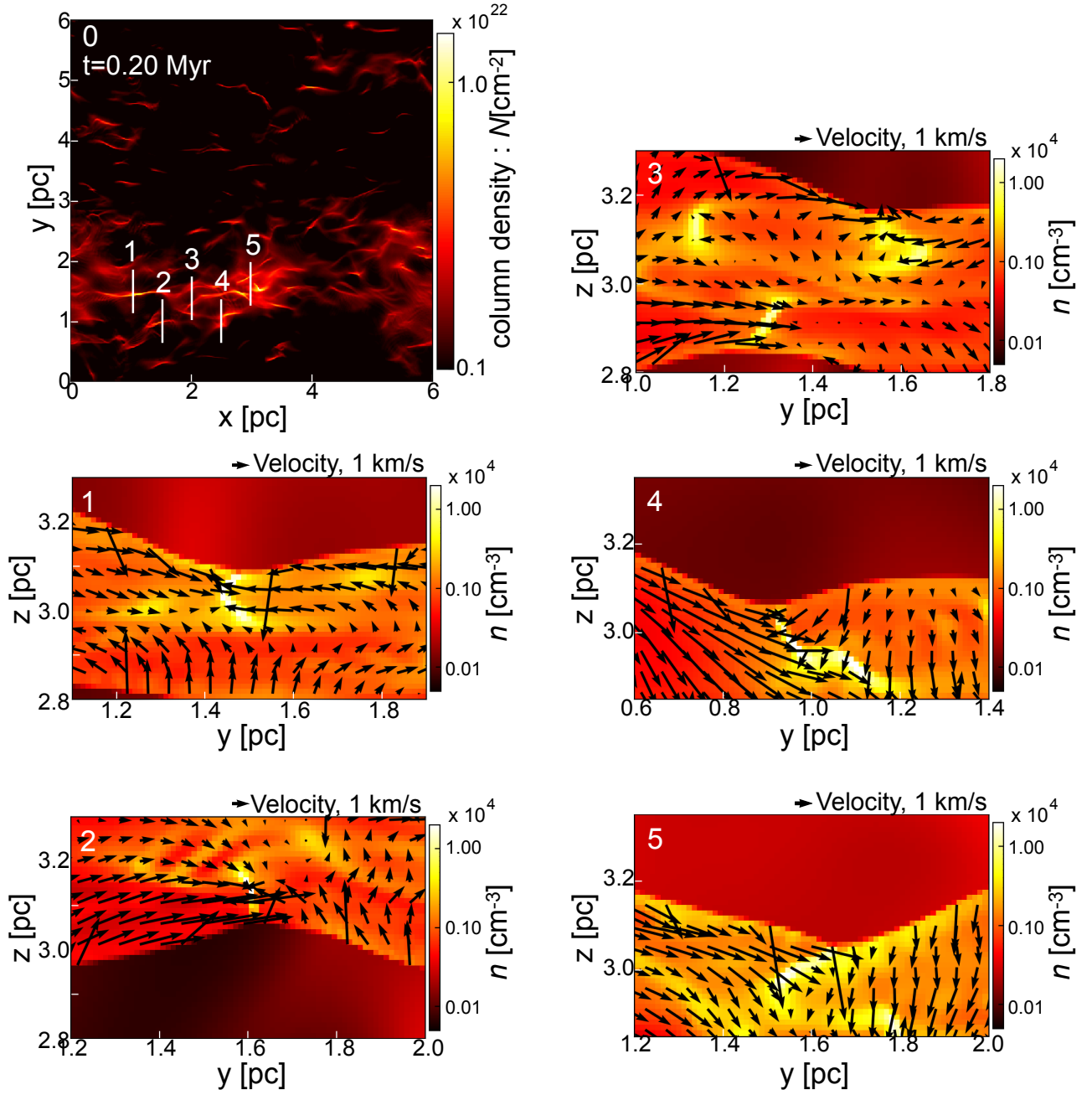


Figure 5. Same as Figure 4 but for model v12GyTy. We can confirm that the oblique MHD shock compression mechanism takes a major role in the filament formation even in the case of initial turbulence with high shock velocity.

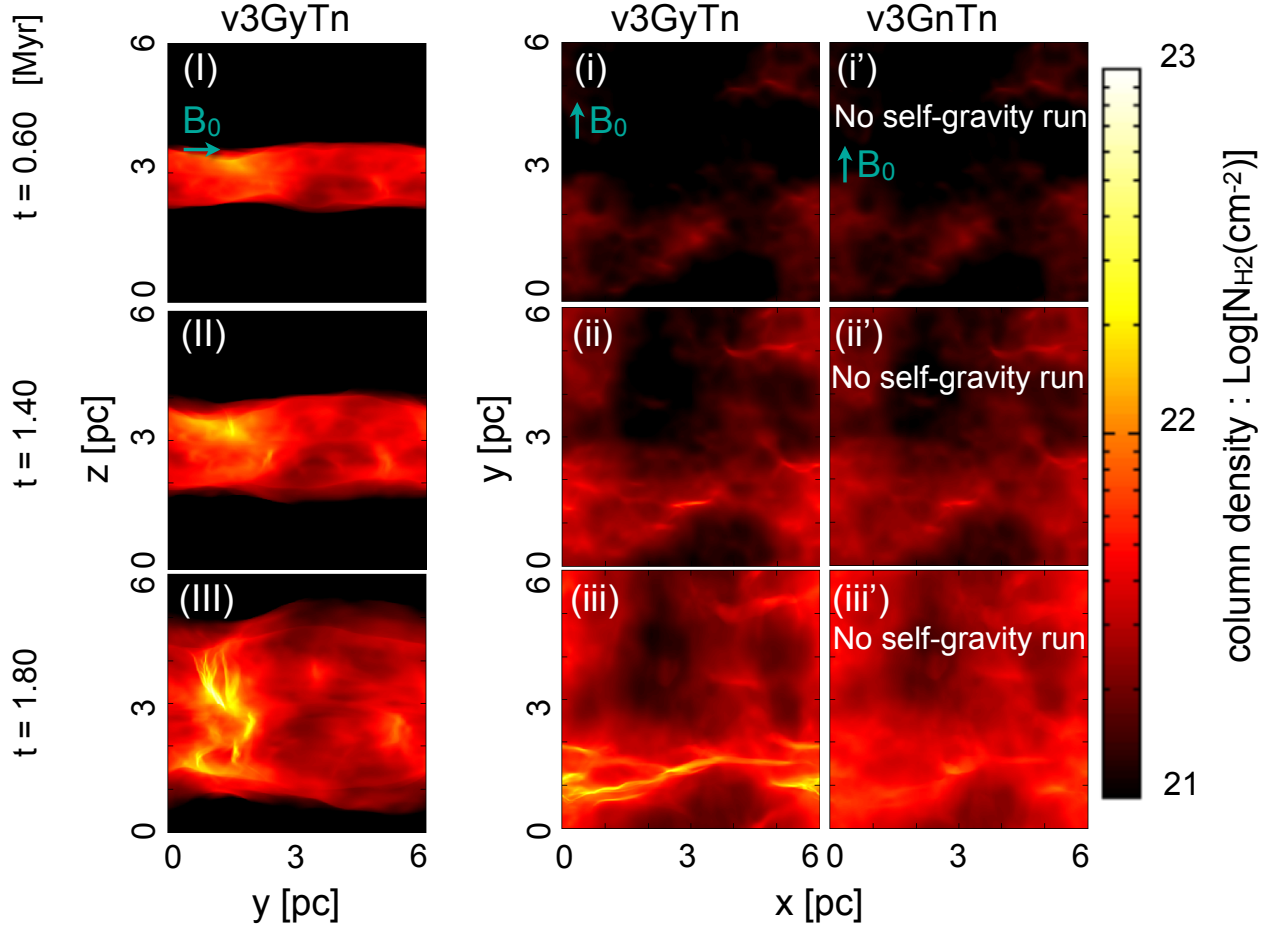


Figure 6. Column density maps at time $t = 0.6$ (top), 1.4 (middle), and 1.8 (bottom) Myr. *Left row* (panels I, II, and III): Column density in the y - z plane of model v3GyTn. *Middle row* (panels i, ii, and iii): Same as the panels (I)-(III) but for the x - y plane. *Right row* (panels i', ii', and iii'): Same as the panels (i)-(iii) but for model v3GnTn.

panels (i)-(iii) and (i')-(iii'), more (mostly faint) filaments parallel to the mean magnetic field lines are present compared with that shown in Figure 2. This indicates that initial turbulence helps to create (faint) filaments. By comparing these two models, we again find that self-gravity does not account for the filament formation. However, see below for Figure 8 where we will see that the resulting filaments tend to disperse in the absence of self-gravity.

To clarify the dominant filament formation mechanism, we show the local density cross-sections around the five major filaments as the results of models v12GyTn in Figure 4 and v12GyTy in Figure 5. The high density blobs (yellow regions) in the local cross-section maps correspond to those of the major filaments. In the oblique MHD shock compression mechanism, the post-shock gas flows toward a region behind the concave shock surface, where the filament is formed. Further de-

tails of the flow structure have been reported by Inoue & Fukui (2013) and Inoue et al. (2018). The curved shock morphology and velocity vectors (black arrows) shown in the cross-section panels in both v12GyTn and v12GyTy models clearly support the oblique MHD shock compression mechanism. It should be noted that the concave shock surfaces are clearly visible, particularly in early stage of the filament formation in both simulation and observation (Arzoumanian et al. 2018).

3.2. Low Shock Velocity Case

In Figure 6, we show snapshots at $t = 0.6$ (top), 1.4 (middle), and 1.8 (bottom) Myr of models v3GyTn (panels I-III and i-iii) and v3GnTn (panels i'-iii'). From Eq. (2), the average shock velocity is calculated to be 2.5 km s^{-1} for $v_{\text{coll}} = 3 \text{ km s}^{-1}$ simulations presented in this section. Although filamentary structures are created in panel (iii), no obvious dense filaments are shown

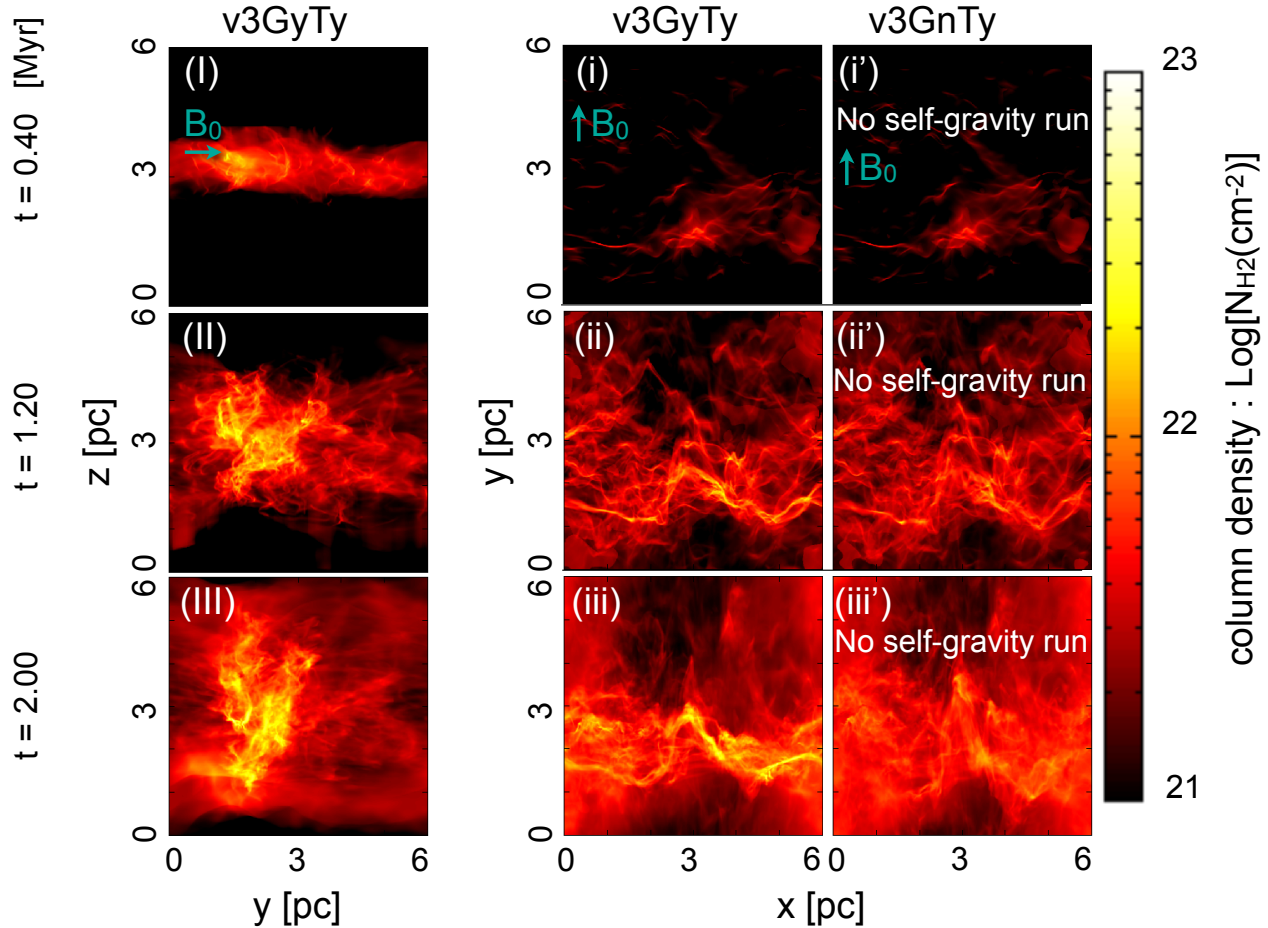


Figure 7. Column density maps at time $t = 0.4$ (top), 1.2 (middle), and 2.0 (bottom) Myr. Left row (panels I, II, and III): Column density in the y - z plane of model v3GyTy. Middle row (panels i, ii, and iii): Same as panels (I)-(III) but for the x - y plane. Right row (panels i', ii', and iii'): Same as panels (i)-(iii) but for model v3GnTy.

in panel (iii'). This suggests that the oblique MHD shock compression mechanism does not work for this low shock velocity case and that self-gravity accounts for the filament formation in model v3GyTn.

Figure 7 shows snapshots at $t = 0.4$ (top), 1.20 (middle), and 2.00 (bottom) Myr of model v3GyTy (panels I-III and i-iii) and the model v3GnTy (panels i'-iii'). The similar filamentary structure formation occurring at $t = 0.4$ and 1.2 Myr in both models suggests that the turbulent filament formation is important for the low shock velocity models². In the later stage of $t = 2.0$ Myr, the results of model v3GyTy show that the filaments are attracted to each other by the self-gravity that eventually induces filament collisions and enhances

the filament line-mass. More detailed analysis is given in §3.4.

3.3. Filament Formation Timescale vs. Free-Fall Time

In this section, we use the following procedure to compute the filament formation time. First, we identify the filaments by employing the FilFinder algorithm (Koch & Rosolowsky 2015) that returns filament skeletons for a given input two-dimensional image. The skeleton is a single-pixel-width object that corresponds to the major-axis of a filament. To focus on major filaments, we neglect filaments having column density smaller than $1.5 \times \bar{N}_{\text{sh}}$, where \bar{N}_{sh} is the mean column density of the shocked region. We confirmed that the result does not change even if we change the factor 1.5 to 2.0. We stress that because of this minimum column density requirement for the filament identification, our analysis given

² Even in the low shock velocity models, some major filaments appear to be formed by the oblique MHD shock mechanism.

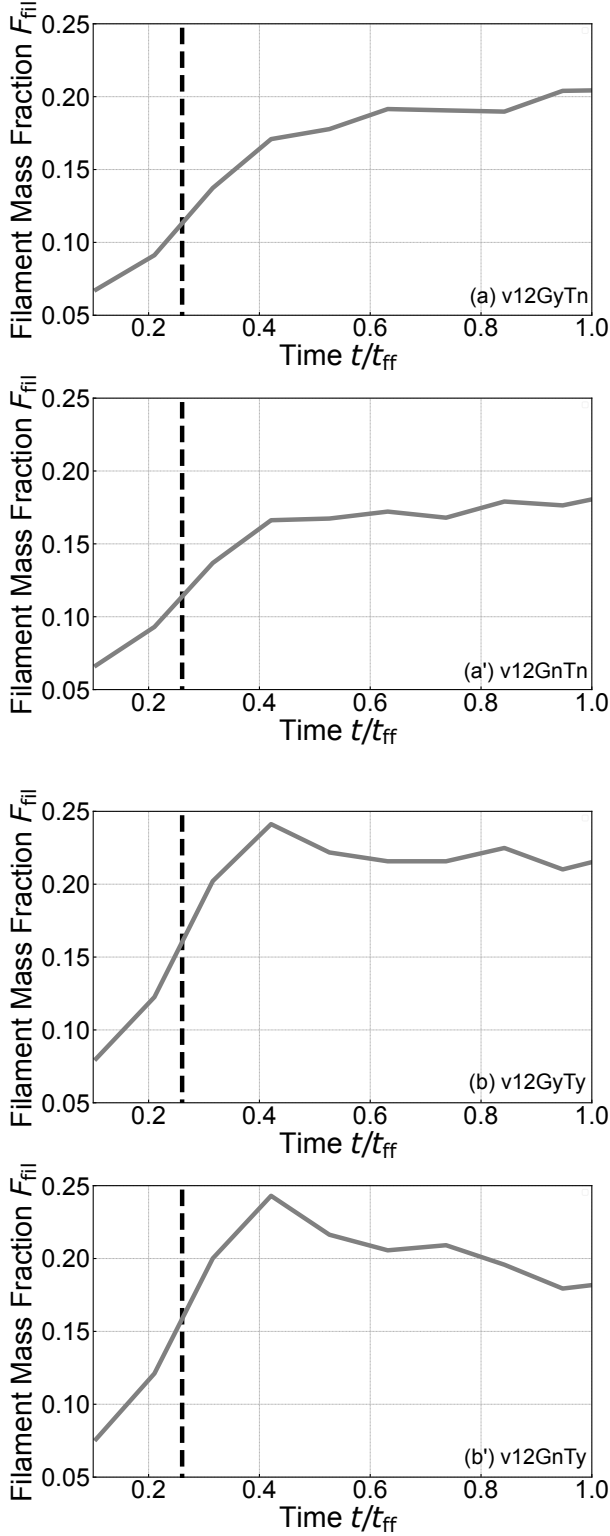


Figure 8. Temporal evolution of the filament mass fraction F_{fil} (solid line) and the filament formation time t_{fil} (dashed line). Panel (a), (a'), (b), and (b') are the results of models v12GyTn, v12GnTn, v12GyTy, and v12GnTy, respectively.

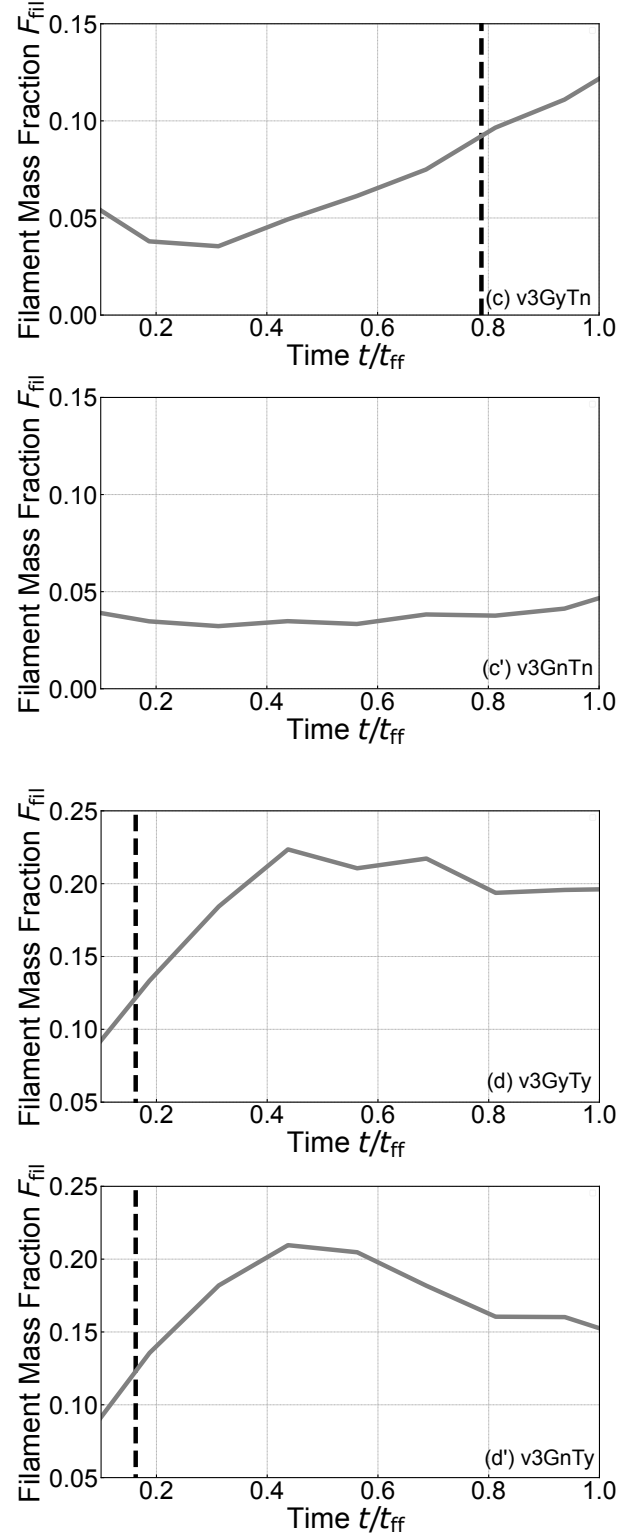


Figure 9. Temporal evolution of the filament mass fraction F_{fil} (solid line) and the filament formation time t_{fil} (dashed line). Panels (c), (c'), (d), and (d') are the results of models v3GyTn, v3GnTn, v3GyTy, and v3GnTy, respectively.

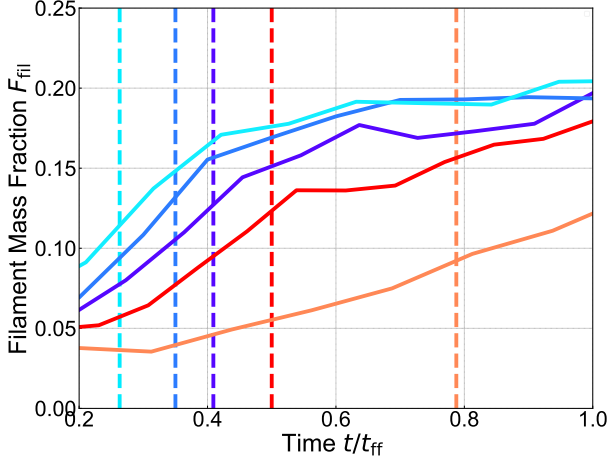


Figure 10. Temporal evolution of the filament mass fraction F_{fil} (solid lines) and the filament formation time t_{fil} (dashed lines) in models with self-gravity and various shock velocities but without turbulent velocity fluctuation. The colors show the results for models v12GyTn (cyan), v10GyTn (blue), v8GyTn (purple), v6GyTn (red), and v3GyTn (orange).

below always omits faint filaments with column densities smaller than $1.5 \times \bar{N}_{\text{sh}}$.

Then, we calculate the filament mass fraction F_{fil} defined by

$$F_{\text{fil}} \equiv M_{\text{fil,tot}}/M_{\text{sh}}, \quad (4)$$

where $M_{\text{fil,tot}}$ and M_{sh} are the total mass of the filaments in the snapshot and the shocked region mass, respectively. $M_{\text{fil,tot}}$ is computed by integrating the gas column density over the region around 0.1 pc of the filament skeleton (Arzoumanian et al. 2011; Koch & Rosolowsky 2015).

Using the F_{fil} , we define the filament formation time t_{fil} as the time at which the filaments are produced most actively. Specifically, The time at which $\Delta F_{\text{fil}}/\Delta t$ reaches its maximum value is defined as the t_{fil} . Where Δt and ΔF_{fil} are the one-tenth of free-fall time t_{ff} in the shocked layer and the increment of F_{fil} in the time interval Δt , respectively.

The free-fall time in the post-shock layer, which gives the timescale of the self-gravitating sheet fragmentation (Nagai et al. 1998), can be estimated as

$$\begin{aligned} t_{\text{ff}} &= \sqrt{\frac{1}{2\pi G \bar{\rho}_1}} \\ &= \sqrt{\frac{\bar{v}_{\text{Alf}}}{2\sqrt{2}\pi G \bar{\rho}_0 \bar{v}_{\text{sh}}}} \\ &= \sqrt{\frac{B_0}{4\sqrt{2}\pi^{3/2} G \bar{\rho}_0^{3/2} (v_{\text{coll}}/2 + B_0/\sqrt{8\pi \bar{\rho}_0})}} \end{aligned}$$

$$\begin{aligned} &\simeq 1.0 \text{ Myr} \left(\frac{B_0}{10 \mu\text{G}} \right)^{1/2} \left(\frac{\bar{n}_0}{100 \text{ cm}^{-3}} \right)^{-3/4} \\ &\times \left[\left(\frac{v_{\text{coll}}}{12 \text{ km/s}} \right) + 0.17 \left(\frac{B_0}{10 \mu\text{G}} \right) \left(\frac{\bar{n}_0}{100 \text{ cm}^{-3}} \right)^{-1/2} \right]^{-1/2} \quad (5) \end{aligned}$$

where $\bar{\rho}_1 \simeq \sqrt{2} \mathcal{M}_A \bar{\rho}_0$ and $\bar{v}_{\text{Alf}} = B_0/\sqrt{4\pi \bar{\rho}_0}$ are the mean density of the shocked layer and the mean Alfvén velocity, respectively (Eq. [1]), and $\bar{v}_{\text{sh}} = v_{\text{coll}}/2 + v_1 \simeq v_{\text{coll}}/2 + B_0/\sqrt{8\pi \bar{\rho}_0}$ represents the mean shock velocity (Eq. [2]).

Figure 8 represents the evolution of the filament mass fraction for the high shock velocity models, in which the time is normalized by the free-fall time t_{ff} . As we have shown in § 3.1, major filaments in these models are created by the oblique MHD shock compression mechanism. Figure 8 confirms that the formation timescale of the filaments by the oblique MHD shock compression mechanism is much faster than the timescale of self-gravity.

Figure 9 shows the evolution of the filament mass fraction for the low shock velocity models. In the results of model v3GyTn (panel c), the filament formation time t_{fil} coincides with the free-fall time $t_{\text{ff}} \simeq 1.6 \text{ Myr}$. This supports our discussion in § 3.2 such that the filaments are created by gravitational fragmentation of the shocked sheet. In panels (d) and (d'), the turbulent filament formation occurs earlier than the free-fall time.

Figure 10 shows the evolution of the filament mass fraction (solid lines) and the filament formation time (dashed lines) for the several shock velocity models without turbulent velocity fluctuation such as v12GyTn (cyan), v10GyTn (blue), v8GyTn (purple), v6GyTn (red), and v3GyTn (orange). We can confirm that the filament formation time increases with decrease in shock velocity, indicating that the dominant formation mechanism of filament gradually changes with a decrease of shock velocity, from oblique MHD shock compression mechanism to self-gravity driven mechanism. Figure 10 suggests threshold collision velocity for the oblique MHD shock compression mechanism is about $v_{\text{coll}} \sim 4.5 \text{ km s}^{-1}$, corresponding to $v_{\text{sh}} \sim 3.3 \text{ km s}^{-1}$.

3.4. Filament Line Mass Function

We calculate the line-mass histogram based on the filament skeletons identified in the previous section. For this purpose, we first determine the direction perpendicular to the filament at each grid on the filament skeleton in the projection plane, and we then compute the line-mass of the filament at each skeleton grid by integrating the gas column density along the normal directions within 0.1 pc from the skeleton grid. Thus, the line-mass evaluated in our histogram is not the average

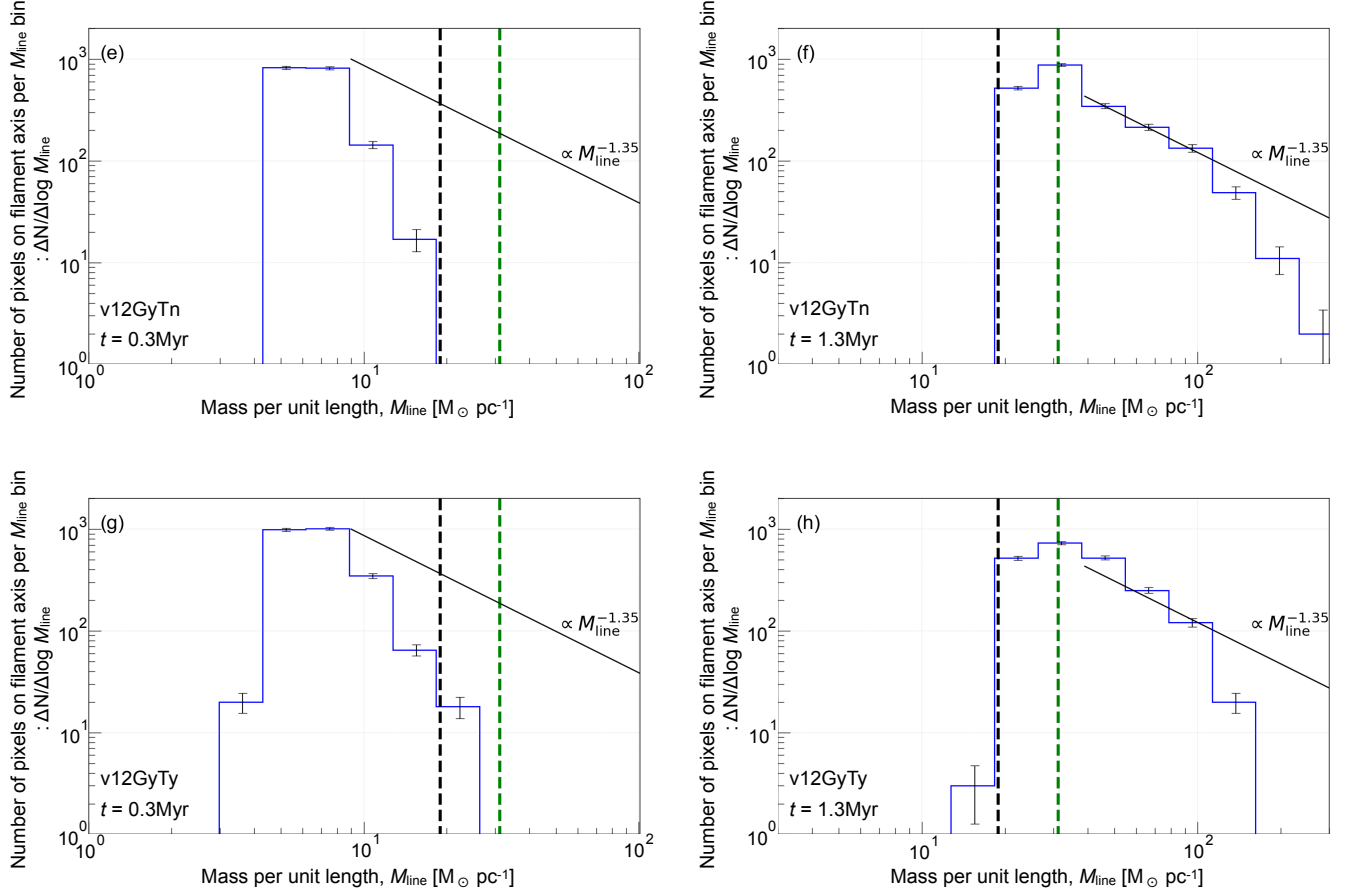


Figure 11. Filament mass functions for model v12GyTn (*top panels* (e) and (f)) and v12GyTy (*bottom panels* (g) and (h)). *Left panels* (e) and (g): Filaments mass functions at time $t = t_{\text{fil}}$. *Right panels* (f) and (h): Results at time $t > 1$ Myr. The black solid line represents the power-law function of the Salpeter initial mass function; the black dashed line shows the critical line-mass (Stodólkiewicz 1963; Ostriker 1964); and the green dashed line is the critical line-mass considering the magnetic field (Tomisaka 2014).

line-mass of each filament but is the local apparent line-mass at each skeleton grid in the 2D projection plane. The histogram is not the real histogram of the number of filaments but the apparent distribution of the projected line-masses.

In the top panels of Figure 11, we plot the line-mass functions of model v12GyTn at $t \simeq t_{\text{fil}}$ (top-left) and a later stage of $t = 1.3$ Myr (top-right). The bottom panels are the same as the top panels but for model v12GyTy. The horizontal and vertical axes are the local line-mass of the filament at a skeleton pixel (or a point on the filament axis) M_{line} and the number of pixels on filament axes (skeletons), respectively. The pixel size equals to $6/512 \text{ pc} \simeq 0.012 \text{ pc}$. The black line represents the power-law function with the Salpeter index, and the green and the black dashed lines show the critical line-mass with and without magnetic field support, respectively, i.e., $M_{\text{line,cr}} = 2c_s^2/G \sim$

$17 M_{\odot} \text{ pc}^{-1}$ (Stodólkiewicz 1963; Ostriker 1964) and

$$\begin{aligned}
 M_{\text{line,cr,B}} &= 2.24 \frac{B_1 w}{G^{1/2}} + 15.4 \frac{c_s^2}{G} \\
 &\simeq 13.5 \left(\frac{w}{0.1 \text{ pc}} \right) \left(\frac{\bar{n}_0}{100 \text{ cm}^{-3}} \right)^{1/2} \\
 &\quad \times \left[\left(\frac{v_{\text{coll}}}{12 \text{ km s}^{-1}} \right) \right. \\
 &\quad \left. + 0.17 \left(\frac{B_0}{10 \mu\text{G}} \right) \left(\frac{\bar{n}_0}{100 \text{ cm}^{-3}} \right)^{-1/2} \right] M_{\odot} \text{ pc}^{-1} \\
 &\quad + 15.4 \left(\frac{c_s}{0.2 \text{ km s}^{-1}} \right)^2 M_{\odot} \text{ pc}^{-1}, \quad (6)
 \end{aligned}$$

derived by Tomisaka (2014), where $B_1 = \sqrt{2} \mathcal{M}_A B_0$ and w are the mean magnetic field in the shocked region and the width of filaments, respectively. It should be noted that Eq. (6) is estimated by using the mean magnetic field strength in the shocked layer, which does not

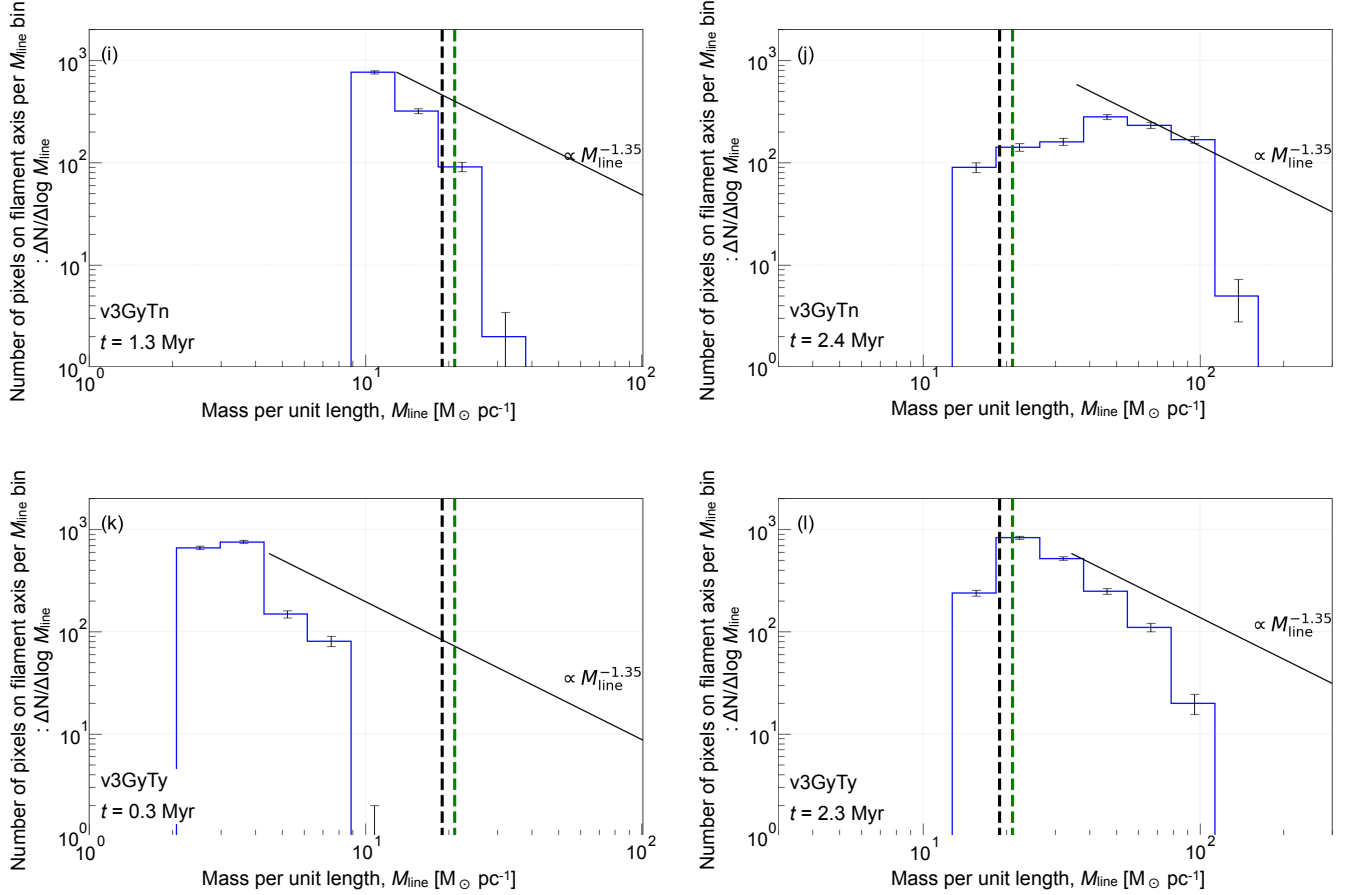


Figure 12. Filament mass functions for model v3GyTn (*top panels* (i) and (j)) and v3GyTy (*bottom panels* (k) and (l)). *Left panels* (i) and (k): Filament mass functions at time $t = t_{\text{fil}}$. *Right panels* (j) and (l): Results at time $t > 2$ Myr. The lines colors are the same as those defined in Figure 11.

give the exact magnetic field strength threading the filaments. In models v12GyTn and v12GyTy, most of the line-masses are sub-critical at $t \simeq t_{\text{fil}}$ (panels (e) and (g) in Figure 11), but they quickly evolve into super-critical ones by continuous accretion flows induced by the oblique shock in roughly 1 Myr (panels (f) and (h) in Figure 11). Recent observations suggest that high line-mass filaments greater than $100 \text{ M}_{\odot} \text{ pc}^{-1}$ are strong candidates for massive star progenitors (Fukui et al. 2019; Shimajiri et al. 2019; Tokuda et al. 2019). We stress that such high line-mass filaments are naturally created in high shock velocity models in a short time.

In Figure 12, we show the filament line-mass function for the low shock velocity cases at $t \simeq t_{\text{fil}}$ (left panels) and at the time when the maximum line-mass exceeds $100 \text{ M}_{\odot} \text{ pc}^{-1}$ (right panels). In the results of model v3GyTn, the filaments have almost critical line-mass at $t = t_{\text{fil}}$ (panel (i)), which is consistent with our finding that the filaments are formed by self-gravity in this model. Panels (k) and (l) for model v3GyTy show

that the turbulent filament formation can create super-critical filaments. However, the formation of massive filaments around $100 \text{ M}_{\odot} \text{ pc}^{-1}$ requires a relatively long time, i.e., more than 2 Myr after $t = t_{\text{fil}}$.

To compare the histograms in models without self-gravity to the ones with self-gravity, in Figure 13, we show line-mass functions for models v12GnTn, v12GnTy, v3GnTn, and v3GnTy. The line-mass functions in Panels (m)-(p) are similar to the ones in panels (e)-(h), respectively. This indicates that star-forming filaments can be created regardless of self-gravity. In panel (t), we can see that low line-mass filaments disappear, and a massive part of filament mass function is truncated comparing to panel (l). This indicates that low line-mass filaments created by turbulence are transient and self-gravity is needed to form massive filaments. It should be noted that we impose a column density threshold of $1.5 \times \bar{N}_{\text{sh}}$ for the filament identification. The threshold column density for the filament identification in model v3GnTy at $t = 2.3$ Myr is set

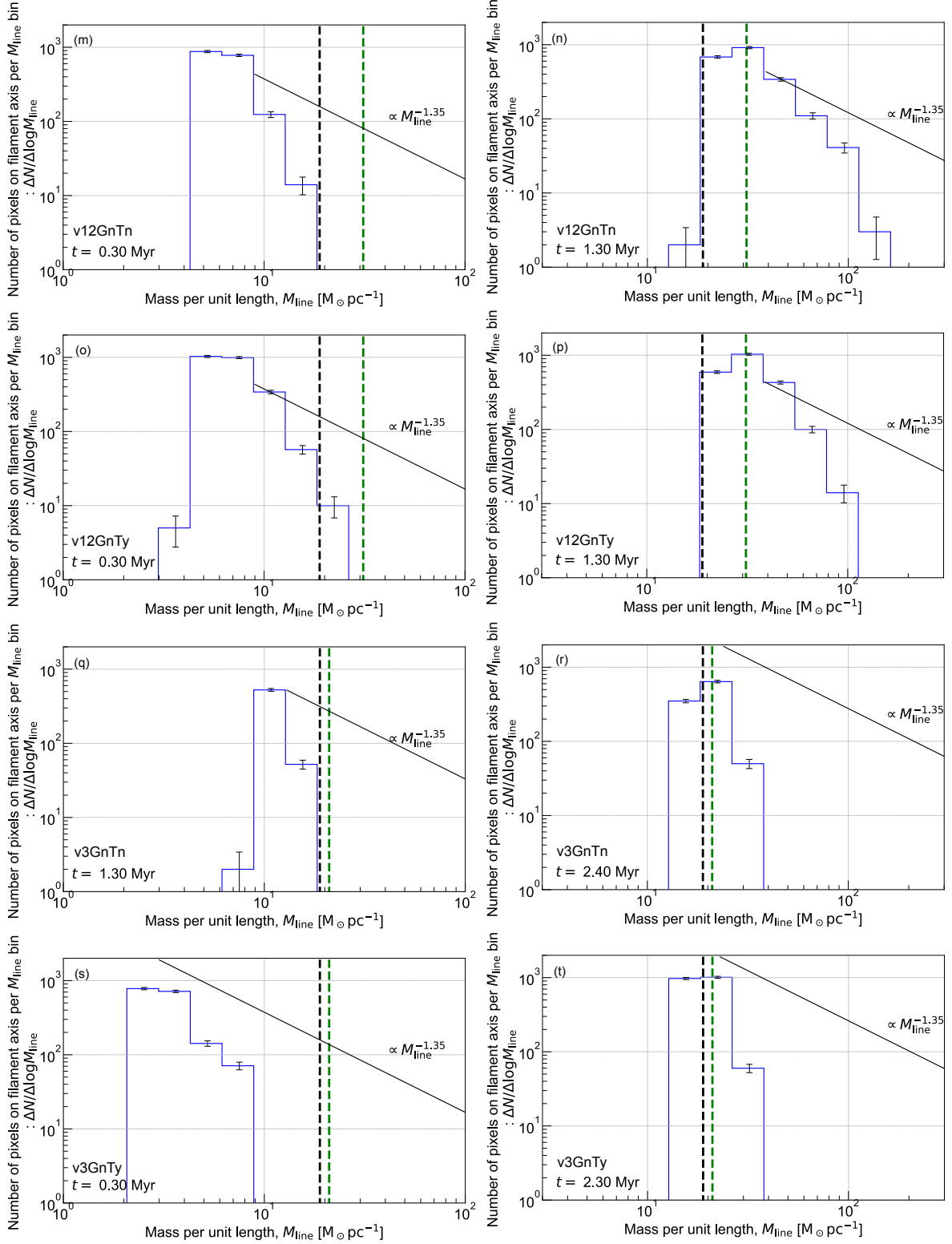


Figure 13. Filament mass functions for no-self-gravitating models v12GnTn (panels m and n), v12GnTy (panels o and p), v12GnTn (panels q and r), and v12GnTy (panels s and t). To compare the histograms in the models with and without self-gravity, we show the histograms that are taken at the same times in Figure 11 and 12. The lines colors are the same as those defined in Figure 11.

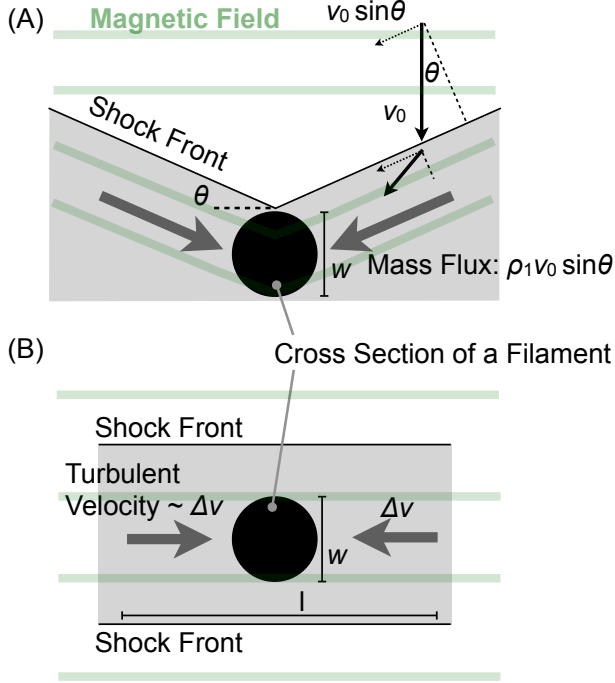


Figure 14. Schematic diagrams of the models used to estimate the filament formation timescale. The gray and black regions represent the post-shock layer and filament, respectively. (A): Schematic diagram of the oblique MHD shock compression mechanism, where w is the filament width, and θ is the oblique shock angle. The angle depends on the detail of the interaction between the shock and the gas clump that evolves into the filament and is roughly $\theta \sim 30^\circ$ as indicated in Figures 4 and 5. (B): Schematic diagram of the turbulent filament formation mechanism, where l is the scale of the turbulent compressive flow related to the velocity of the flow Δv via Larson’s law, and here also we assume the width of the compressive flows as $w = 0.1$ pc.

at $6.5 \times 10^{21} \text{ cm}^{-2}$. The corresponding minimum line-mass of the identified filament is $13 M_\odot \text{ pc}^{-1}$ when the filament width is 0.1 pc.

4. DISCUSSION

In this section, we estimate the growth timescale of the filaments formed by the oblique shock and turbulent formation mechanisms, which explain why the dominant filament formation mechanism changes with shock velocity. First, we estimate the filament formation timescale in the oblique MHD shock compression mechanism. As shown schematically in panel (A) of Figure 14, the oblique MHD shock model predicts that the mass flux of the post-shock gas flow to the filament is given by $\sim \rho_1 v_0 \sin \theta$, where θ is the oblique shock angle, and we have used the fact that the velocity component perpendicular to the shock normal is almost conserved

across the shock³. If we assume constant width w of the filament, the line-mass of the filament after time t can be written as

$$M_{\text{line}} = 2\rho_1 v_0 w t \sin \theta. \quad (7)$$

By substituting the isothermal strong MHD shock jump condition $\rho_1 \simeq \sqrt{2}\mathcal{M}_A\rho_0$ (Eq. [1]), the timescale t_O , in which the oblique shock mechanism creates filament of the line-mass M_{line} , is estimated in the following equation, where $v_0 = v_{\text{sh}}$.

$$\begin{aligned} t_O &= \frac{M_{\text{line}}}{2\rho_1 v_0 \sin \theta w} \\ &= \frac{M_{\text{line}} B_0}{4\sqrt{2}\pi\rho_0^{3/2} v_0^2 w \sin \theta} \\ &= 0.3 \text{ Myr } (\sin \theta)^{-1} \left(\frac{v_{\text{sh}}}{7 \text{ km s}^{-1}} \right)^{-2} \\ &\quad \times \left(\frac{M_{\text{line}}}{M_{\text{line,cr}}} \right) \left(\frac{n_0}{100 \text{ cm}^{-3}} \right)^{-3/2} \left(\frac{B_0}{10 \mu\text{G}} \right) \left(\frac{w}{0.1 \text{ pc}} \right)^{-1} \end{aligned} \quad (8)$$

Next, we consider the timescale of the turbulent filament formation. As shown in panel (B) in Figure 14, the filament is formed when a turbulent flow converges in the shock-compressed slab. In the following equation, we write the velocity of the converging flows as Δv , their scale as l , and the width of the flow as h . Because the origin of the converging flow is turbulence, we choose Larson’s law $\Delta v \sim V_{08} (l/L_1)^{0.5}$, where $V_{08} = 0.8 \text{ km s}^{-1}$, and $L_1 = 1 \text{ pc}$ (Larson 1981). Then, the mass accumulation timescale is given by

$$t_T = l/\Delta v \sim l^{1/2} L_1^{1/2} / V_{08}. \quad (9)$$

By using l and w , we can estimate the line mass of the filament as

$$M_{\text{line}} = \rho_1 l w. \quad (10)$$

By combining, Eqs (9)-(10), the timescale t_T , in which the turbulent flow creates filament of the line-mass M_{line} , can be estimated using the following equation.

$$\begin{aligned} t_T &= \frac{M_{\text{line}}}{\rho_1 w \Delta v} \\ &= \left(\frac{M_{\text{line}} L_1 B_0}{2\sqrt{2}\pi w V_{08}^2 \rho_0^{3/2} v_{\text{sh}}} \right)^{1/2} \\ &= 0.78 \text{ Myr } \left(\frac{v_{\text{sh}}}{7 \text{ km s}^{-1}} \right)^{-1/2} \left(\frac{M_{\text{line}}}{M_{\text{line,cr}}} \right)^{1/2} \\ &\quad \times \left(\frac{w}{0.1 \text{ pc}} \right)^{-1/2} \left(\frac{\bar{n}_0}{100 \text{ cm}^{-3}} \right)^{-3/4} \left(\frac{B_0}{10 \mu\text{G}} \right)^{1/2} \end{aligned} \quad (11)$$

³ The conservation of the parallel velocity component is exact only for the limit of no magnetic field. In the case of fast shock, the parallel velocity conservation is a highly accurate approximation.

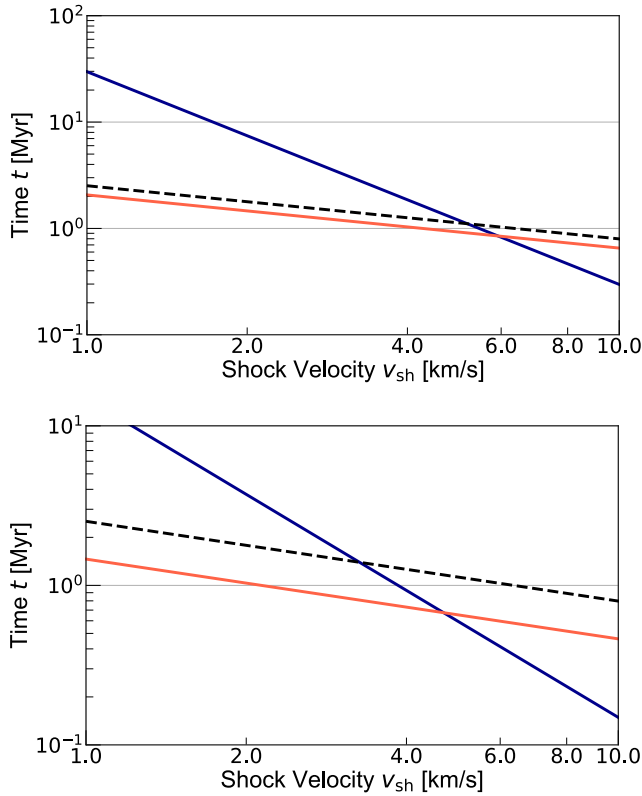


Figure 15. Filament formation timescales as functions of shock velocity. The blue line shows the timescale for the oblique shock mechanism given by Eq. (8), and the red line shows turbulent filament formation timescale estimated by Eq. (11). The dashed line represents the free-fall time in the shocked region t_{ff} (Eq. 5). *Top panel:* Timescales required to reach the thermal critical line mass (e.g., Stodólkiewicz 1963; Ostriker 1964), i.e., $M_{\text{line}}(t) = M_{\text{line,cr}}$. *Bottom panel:* Timescales required to reach half the thermal critical line mass, i.e., $M_{\text{line}}(t) = M_{\text{line,cr}}/2$.

Here, we use $V_{08} = 0.8 \text{ km s}^{-1}$ and $L_1 = 1 \text{ pc}$.

In the top panel of Figure 15, we plot the two timescales t_O and t_T for the critical line-mass filament ($M_{\text{line}} = M_{\text{line,cr}}$) as a function of the shock velocity. We also plot the timescales for the filament with half the critical line-mass ($M_{\text{line}} = M_{\text{line,cr}}/2$) in the bottom panel. The blue lines represent t_O with $\theta = 30^\circ$; the red lines are t_T with $f = 0.5$; and dashed lines are the free-fall time in the post-shock layer (Eq. 5). When the shock velocity is high ($v_{\text{sh}} \gtrsim 5 \text{ km s}^{-1}$, i.e., $v_{\text{coll}} \gtrsim 8 \text{ km s}^{-1}$), we obtain the relationship of $t_O < t_T < t_{\text{ff}}$,

and for the lower shock velocity cases ($v_{\text{sh}} \lesssim 5 \text{ km s}^{-1}$, i.e., $v_{\text{coll}} \lesssim 8 \text{ km s}^{-1}$), we get $t_T < t_{\text{ff}} < t_O$. These results are fairly consistent with the results of the simulations. That is, the oblique MHD shock compression mechanism is important for the high shock velocity case, whereas the turbulent filament formation is more effective for the low shock velocity case.

5. SUMMARY

We have performed a series of isothermal MHD simulations of the filament formation triggered by shock compression of a molecular cloud. We found that when the shock is fast ($v_{\text{sh}} \simeq 7 \text{ km s}^{-1}$), the oblique shock mechanism proposed by Inoue & Fukui (2013) works as the major mechanism for the formation of star-forming filaments irrespective of the presence of the turbulence and self-gravity. When the shock is slow ($v_{\text{sh}} \simeq 2.5 \text{ km s}^{-1}$), compressive flows involved in supersonic turbulence induce transient filament formation but the resulting filaments disperse unless the line-masses are comparable or larger than the thermal critical line-mass. When the shock velocity is low and no turbulence is set initially, the fragmentation of the shock-compressed sheet by self-gravity creates filaments over the gravitational fragmentation timescale of the dense sheet. Moreover, we analyzed the line-mass distribution of the filaments and showed that strong shock waves can naturally create high-line-mass filaments such as those observed in the massive star-forming regions ($M_{\text{line}} \gtrsim 100 M_\odot \text{ pc}^{-1}$) in a short time. We stress that such high line-mass filaments are naturally created in high shock velocity models in a timescale of the creation of dense compressed sheet-like region. We conclude that the dominant filament formation mode changes with the strength of the incident shock wave.

6. ACKNOWLEDGMENTS

We thank K. Iwasaki and D. Arzoumanian for fruitful discussions. The numerical computations were carried out on XC50 system at the Center for Computational Astrophysics (CfCA) of National Astronomical Observatory of Japan. This work is supported by Grant-in-aids from the Ministry of Education, Culture, Sports, Science, and Technology (MEXT) of Japan (15K05039, 18H05436).

REFERENCES

- André, P., Men'shchikov, A., Bontemps, S., et al. 2010, *A&A*, 518, L102, doi: [10.1051/0004-6361/201014666](https://doi.org/10.1051/0004-6361/201014666)
- Arzoumanian, D., Shimajiri, Y., Inutsuka, S.-i., Inoue, T., & Tachihara, K. 2018, *PASJ*, 70, 96, doi: [10.1093/pasj/psy095](https://doi.org/10.1093/pasj/psy095)

- Arzoumanian, D., André, P., Didelon, P., et al. 2011, *A&A*, 529, L6, doi: [10.1051/0004-6361/201116596](https://doi.org/10.1051/0004-6361/201116596)
- Balfour, S. K., Whitworth, A. P., & Hubber, D. A. 2017, *MNRAS*, 465, 3483, doi: [10.1093/mnras/stw2956](https://doi.org/10.1093/mnras/stw2956)
- Balfour, S. K., Whitworth, A. P., Hubber, D. A., & Jaffa, S. E. 2015, *MNRAS*, 453, 2471, doi: [10.1093/mnras/stv1772](https://doi.org/10.1093/mnras/stv1772)
- Beresnyak, A., Lazarian, A., & Cho, J. 2005, *ApJL*, 624, L93, doi: [10.1086/430702](https://doi.org/10.1086/430702)
- Chen, C.-Y. 2015, PhD thesis, 1, <https://arxiv.org/abs/arXiv:1508.02710v1>
- Chen, C. Y., & Ostriker, E. C. 2014, *ApJ*, 785, doi: [10.1088/0004-637X/785/1/69](https://doi.org/10.1088/0004-637X/785/1/69)
- Crutcher, R. M. 2012, *ARA&A*, 50, 29, doi: [10.1146/annurev-astro-081811-125514](https://doi.org/10.1146/annurev-astro-081811-125514)
- Dedner, A., Kemm, F., Kröner, D., et al. 2002, *JCoPh*, 175, 645, doi: [10.1006/jcph.2001.6961](https://doi.org/10.1006/jcph.2001.6961)
- Elmegreen, B. G., & Scalo, J. 2004, *ARA&A*, 42, 211, doi: [10.1146/annurev.astro.41.011802.094859](https://doi.org/10.1146/annurev.astro.41.011802.094859)
- Enoch, M. L., Glenn, J., Evans, Neal J., I., et al. 2007, *ApJ*, 666, 982, doi: [10.1086/520321](https://doi.org/10.1086/520321)
- Federrath, C. 2016, *MNRAS*, 457, 375, doi: [10.1093/mnras/stv2880](https://doi.org/10.1093/mnras/stv2880)
- Fukui, Y., Habe, A., Inoue, T., Enokiya, R., & Tachihara, K. 2020, arXiv e-prints, arXiv:2009.05077, <https://arxiv.org/abs/2009.05077>
- Fukui, Y., Tokuda, K., Saigo, K., et al. 2019, *ApJ*, 886, 14, doi: [10.3847/1538-4357/ab4900](https://doi.org/10.3847/1538-4357/ab4900)
- Heiles, C., & Crutcher, R. 2005, *Cosm. Magn. Fields*, 137, doi: [10.1007/11369875_7](https://doi.org/10.1007/11369875_7)
- Hennebelle, P. 2013, *A&A*, 556, A153, doi: [10.1051/0004-6361/201321292](https://doi.org/10.1051/0004-6361/201321292)
- Heyer, M. H., & Brunt, C. M. 2004, *ApJL*, 615, L45, doi: [10.1086/425978](https://doi.org/10.1086/425978)
- Inoue, T., & Fukui, Y. 2013, *ApJL*, 774, doi: [10.1088/2041-8205/774/2/L31](https://doi.org/10.1088/2041-8205/774/2/L31)
- Inoue, T., Hennebelle, P., Fukui, Y., et al. 2018, *PASJ*, 70, 1, doi: [10.1093/pasj/psx089](https://doi.org/10.1093/pasj/psx089)
- Inoue, T., & Inutsuka, S.-i. 2012, *ApJ*, 759, 35, doi: [10.1088/0004-637X/759/1/35](https://doi.org/10.1088/0004-637X/759/1/35)
- . 2016, *ApJ*, 833, 10, doi: [10.3847/0004-637X/833/1/10](https://doi.org/10.3847/0004-637X/833/1/10)
- Kitsionas, S., & Whitworth, A. P. 2007, *MNRAS*, 378, 507, doi: [10.1111/j.1365-2966.2007.11707.x](https://doi.org/10.1111/j.1365-2966.2007.11707.x)
- Koch, E. W., & Rosolowsky, E. W. 2015, *MNRAS*, 452, 3435, doi: [10.1093/mnras/stv1521](https://doi.org/10.1093/mnras/stv1521)
- Könyves, V., André, P., Men'shchikov, A., et al. 2015, *A&A*, 584, A91, doi: [10.1051/0004-6361/201525861](https://doi.org/10.1051/0004-6361/201525861)
- Lada, C. J., Lombardi, M., & Alves, J. F. 2010, *ApJ*, 724, 687, doi: [10.1088/0004-637X/724/1/687](https://doi.org/10.1088/0004-637X/724/1/687)
- Larson, R. B. 1981, *MNRAS*, 194, 809, doi: [10.1093/mnras/194.4.809](https://doi.org/10.1093/mnras/194.4.809)
- Matsumoto, T. 2007, *PASJ*, 59, 905, doi: [10.1093/pasj/59.5.905](https://doi.org/10.1093/pasj/59.5.905)
- Matsumoto, T., Dobashi, K., & Shimoikura, T. 2015, *ApJ*, 801, doi: [10.1088/0004-637X/801/2/77](https://doi.org/10.1088/0004-637X/801/2/77)
- Miyama, S. M., Narita, S., & Hayashi, C. 1987a, *PThPh*, 78, 1051, doi: [10.1143/PTP.78.1051](https://doi.org/10.1143/PTP.78.1051)
- . 1987b, *PThPh*, 78, 1273, doi: [10.1143/PTP.78.1273](https://doi.org/10.1143/PTP.78.1273)
- Miyoshi, T., & Kusano, K. 2005, *JCoPh*, 208, 315, doi: [10.1016/j.jcp.2005.02.017](https://doi.org/10.1016/j.jcp.2005.02.017)
- Nagai, T., Inutsuka, S., & Miyama, S. M. 1998, *ApJ*, 506, 306, doi: [10.1086/306249](https://doi.org/10.1086/306249)
- Ostriker, J. 1964, *ApJ*, 140, 1056, doi: [10.1086/148005](https://doi.org/10.1086/148005)
- Padoan, P., & Nordlund, A. 1999, *ApJ*, 526, 279, doi: [10.1086/307956](https://doi.org/10.1086/307956)
- Planck Collaboration XXXV. 2016, *A&A*, 586, A138, doi: [10.1051/0004-6361/201525896](https://doi.org/10.1051/0004-6361/201525896)
- Scalo, J., & Elmegreen, B. G. 2004, *ARA&A*, 42, 275, doi: [10.1146/annurev.astro.42.120403.143327](https://doi.org/10.1146/annurev.astro.42.120403.143327)
- Shimajiri, Y., André, P., Ntormousi, E., et al. 2019, *A&A*, 632, A83, doi: [10.1051/0004-6361/201935689](https://doi.org/10.1051/0004-6361/201935689)
- Stodólkiewicz, J. S. 1963, *AcA*, 13, 30
- Tokuda, K., Fukui, Y., Harada, R., et al. 2019, *ApJ*, 886, 15, doi: [10.3847/1538-4357/ab48ff](https://doi.org/10.3847/1538-4357/ab48ff)
- Tomisaka, K. 2014, *ApJ*, 785, doi: [10.1088/0004-637X/785/1/24](https://doi.org/10.1088/0004-637X/785/1/24)
- Tomisaka, K., & Ikeuchi, S. 1983, *PASJ*, 35, 187
- Vaidya, B., Hartquist, T. W., & Falle, S. A. E. G. 2013, *MNRAS*, 433, 1258, doi: [10.1093/mnras/stt800](https://doi.org/10.1093/mnras/stt800)